

EARTH PRESSURE FIELD MODELING FOR TUNNEL FACE STABILITY EVALUATION OF EPB SHIELD MACHINES BASED ON OPTIMIZATION SOLUTION

YI AN^{a,*}, ZHUOHAN LI^a, CHANGZHI WU^b
HUOSHENG HU^c, CHENG SHAO^a AND BO LI^a

^aSchool of Control Science and Engineering
Dalian University of Technology
Dalian 116024, China

^bSchool of Management, Guangzhou University
Guangzhou 510006, China

^cSchool of Computer Science and Electronic Engineering
University of Essex
Colchester CO4 3SQ, United Kingdom

ABSTRACT. Earth pressure balanced (EPB) shield machines are large and complex mechanical systems and have been widely applied to tunnel engineering. Tunnel face stability evaluation is very important for EPB shield machines to avoid ground settlement and guarantee safe construction during the tunneling process. In this paper, we propose a novel earth pressure field modeling approach to evaluate the tunnel face stability of large and complex EPB shield machines. Based on the earth pressures measured by the pressure sensors on the clapboard of the chamber, we construct a triangular mesh model for the earth pressure field in the chamber and estimate the normal vector at each measuring point by using optimization solution and projection Delaunay triangulation, which can reflect the change situation of the earth pressures in real time. Furthermore, we analyze the characteristics of the active and passive earth pressure fields in the limit equilibrium states and give a new evaluation criterion of the tunnel face stability based on Rankine's theory of earth pressure. The method validation and analysis demonstrate that the proposed method is effective for modeling the earth pressure field in the chamber and evaluating the tunnel face stability of EPB shield machines.

1. Introduction.

1.1. EPB shield machine. Shield machines are large and complex mechanical systems and have been widely applied to the construction of tunnel projects, such as railways, subways, and municipal facilities. With the rapid development of shield technology, different kinds of shield machines rise in response to the proper time and conditions, as shown in Figure 1. According to working principles, shield machines are categorized into three kinds: earth pressure balanced shield machines, slurry shield machines, and hard rock shield machines. Different kinds of geological conditions need different kinds of shield machines in tunnel excavation projects. The earth pressure balanced (EPB) shield machines are mainly used in cohesive soils

2010 *Mathematics Subject Classification.* Primary: 62P30.

Key words and phrases. Earth pressure, shield machine, normal vector, triangular mesh, tunnel face stability.

* Corresponding author: Yi An (Email: anyi@dlut.edu.cn).

with high clay contents and low water permeability. They use the excavated soil in the chamber directly as the support medium to maintain the tunnel face stability. When the earth pressure in the chamber equals the pressure of the surrounding soil, the necessary balance has been achieved and the tunnel face is stable. In the geological condition with high ground water pressure and high water permeability, such as saturated grained soils, the slurry shield machines are usually used, and the support pressure in the chamber is precisely managed by using an automatically controlled air cushion. The hard rock shield machines are mainly used in the geological condition of hard rock, and they use the cutter head to break rock. In this paper, we only study the EPB shield machines. Figure 2 shows the structure of the EPB shield machine, which is composed of the cutter head, chamber, clapboard, advance jack, screw conveyer, segment erector, and shell.

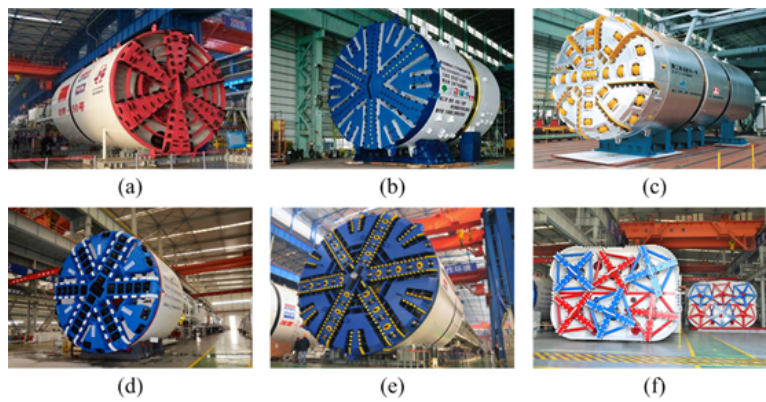


FIGURE 1. Different kinds of shield machines. (a) Earth pressure balance shield machine. (b) Slurry shield machine. (c) Hard rock shield machine. (d) Mixed shield machine. (e) Dual mode shield machine. (f) Rectangle shield machine.

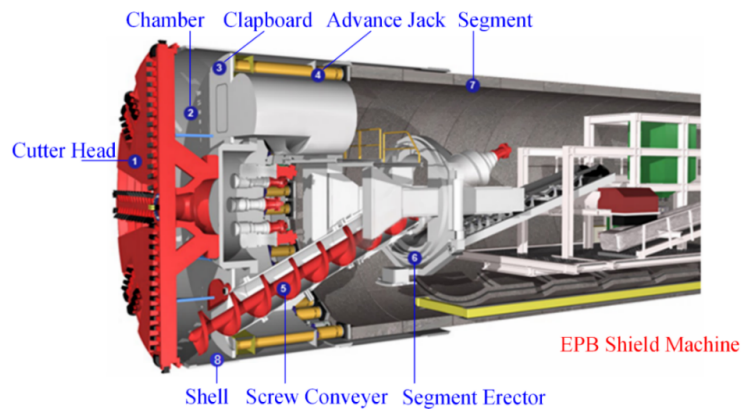


FIGURE 2. Structure of the EPB shield machine.

During the tunneling process, the soil in front of the tunnel face is excavated into the chamber by the cutter head constantly. At the same time, stirring of the blender and injecting of the improver make the excavated soil fill up the chamber uniformly. Then, the soil is discharged out of the chamber by the screw conveyer. In order to maintain tunnel face stability and avoid ground settlement, the EPB shield machine must achieve a balance between the earth pressure in the chamber and the earth and hydrostatic pressures in front of the tunnel face, as shown in Figure 3. Generally, the earth pressure in the chamber can be adjusted by controlling the soil mass discharged out of the chamber and the soil mass cut into the chamber. This is achieved by controlling the screw conveyer speed and excavation advance speed. The pressure distributions along both sides of the tunnel face are roughly trapezoidal. The pressure at the top of the tunnel face is smaller, and the pressure at the bottom of the tunnel face is larger, as shown in Figure 3.

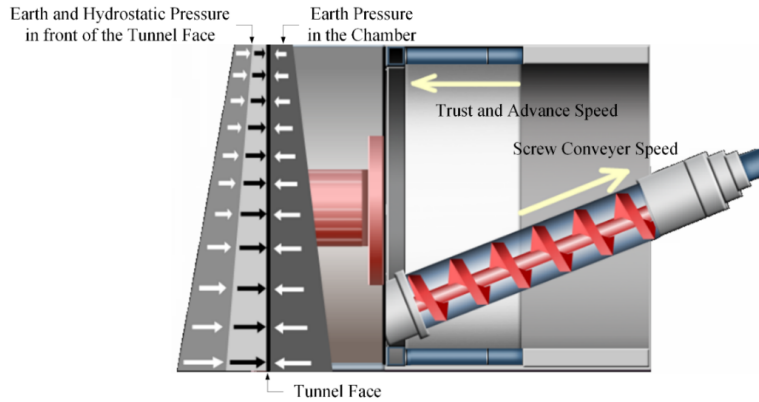


FIGURE 3. Working principle of the EPB shield machine.

1.2. Tunnel face stability. In order to maintain tunnel face stability, the earth pressure (support pressure) in the chamber must balance the external earth and hydrostatic pressures. Otherwise, the tunnel face may lose its stability, which will lead to ground deformation. For example, too low a support pressure may run the risk of collapse (active failure), and too high a support pressure may result in blow-out (passive failure) [20]. Thus, the evaluation of tunnel face stability is essential to the safe construction of shield tunnels. Through the stability analysis and evaluation, we may determine an appropriate support pressure which can prevent the collapse and the blow-out of the soil mass near the tunnel face. In the past 30 years, many researchers have devoted themselves to developing methods to estimate the support pressure to stabilize the tunnel face in different situations. Generally, these methods can be categorized into three types: analytical methods, experimental methods, and numerical methods.

The analytical methods are mainly based on limit analysis and limit equilibrium. In the limit analysis methods, the upper and lower bound theorems are used to derive the support pressure. Li *et al.* [20] investigated the face stability of a large slurry shield-driven tunnel in soft clay by using an upper bound approach in limit analysis. Atkinson and Potts [4] derived the safe and unsafe tunnel support pressures (the

lower and upper bounds to the collapse load) for a circular tunnel in cohesionless soil. Davis *et al.* [12] used the limit theorems of plasticity to obtain lower and upper bound stability solutions against collapse and blow-out for a shallow tunnel in cohesive material. Leca and Dormieux [19] derived the lower and upper bound solutions against collapse and blow-out for a circular tunnel in frictional material. Augarde *et al.* [5] used the finite element limit analysis based on classical plasticity theory to derive the lower and upper bounds for a plain strain heading in undrained soil conditions. Ibrahim *et al.* [14] presented a 3D failure mechanism for a circular tunnel in the dry multilayered purely frictional soil based on the upper bound limit analysis method. Pan and Dias [23] researched the face stability of a circular tunnel in weak rock masses under the water table based on an advanced 3D rotational collapse mechanism in the context of the kinematical approach of limit analysis. Huang *et al.* [13] proposed a new numerical upper-bound method for three-dimensional stability problems in undrained clay to analyze the tunnel face stability. Different from the limit analysis methods, in the limit equilibrium methods, tunnel face stability is evaluated by considering the limit equilibrium of a three-dimensional wedge model which consists of a wedge and a prism with slip planes. Jancsecz and Steiner [15] used a limit state model to determine the required support pressure to balance the earth and water pressures in front of the tunnel face. Anagnostou and Kovári [2] applied a wedge model to analyze the mechanism of face failure and study the time-dependent effects of slurry infiltration into the ground ahead of the tunnel face on the tunnel face stability for slurry shields. Two years later, they used the same model to analyze the mechanism of face failure and calculated the effective support pressure under the drained conditions for EPB shields [3]. Broere [9] constructed a multilayer wedge model to analyze the tunnel face stability under heterogeneous soil conditions. In conclusion, the analytical methods theoretically analyze the failure mechanisms and derive the required support pressures under different kinds of soil conditions.

In recent years, experimental methods have been widely developed for analyzing the tunnel face stability. Chambon and Corté [10] conducted a series of centrifugal model tests to analyze the tunnel face stability in cohesionless soil, and investigated the limit internal support pressures for various conditions. Kirsch [18] performed small-scale model tests to investigate the mechanism of face failure and the support pressure for a shallow tunnel in dry sand. Ahmed and Iskander [1] carried out transparent soil model tests to measure the tunnel face support pressure and the associated soil deformations in saturated sand. Lü *et al.* [21] carried out nine physical model tests to understand the failure mechanism and limit support pressure of a shield tunnel face under seepage condition.

With the rapid development of numerical calculation, many researchers have used the numerical methods, such as finite element methods and discrete element methods, to analyze tunnel face stability. Schuller and Schweiger [25] applied a multilaminate model to numerically simulate tunnel excavation by using finite element analysis. It was demonstrated that a realistic failure mechanism which involves the formation of shear bands can be simulated for tunnel excavation in soil with low overburden. Borja [8] presented a finite element model for strain localization analysis of elastoplastic solids subjected to discontinuous displacement fields, which can also be used for analyzing tunnel face stability. Kim and Tonon [17] employed three-dimensional finite element simulations to investigate the effects of tunnel diameter, cover-to-diameter ratio, lateral earth pressure coefficient, and soil strength

parameters on the stability and displacements of the tunnel face of shield driven tunnels in drained conditions. Michael *et al.* [22] developed a 3D finite element model for shield EPB tunnelling to analysis the tunnel face stability. Besides finite element analysis, discrete element analysis is often used in the analysis of tunnel face stability. Karim [16] carried out a series of three-dimensional discrete element simulations of tunnel face failure in sand. Chen *et al.* [11] used the discrete element method to investigate the failure mechanism and the limit support pressure of a tunnel face in dry sand ground.

1.3. The proposed approach. The above-mentioned different kinds of methods are mainly to analyze the mechanism of tunnel face stability for shield machines in various soil conditions. Generally, these research results are achieved under some assumptions and idealized conditions, and provide a good theoretical foundation for maintaining tunnel face stability. However, in real construction process, the tunnel face stability is mainly evaluated online by using the earth pressure values measured by the pressure sensors installed on the clapboard of the chamber. The operators tend to average the measured earth pressures in the chamber, and use the average earth pressure and the classical earth pressure theory to evaluate tunnel face stability. If the average earth pressure in the chamber is between the active earth pressure and the passive earth pressure, the tunnel face is stable; if not, the tunnel face is unstable [27]. However, this evaluation method simplifies the earth pressures in different positions of the chamber to an average earth pressure, does not consider the whole change situation of the earth pressures in the chamber, neglects the whole support action to the tunnel face, and needs the operators to have rich experience to make an accurate judgment.

In fact, with the incoming and outgoing of the soil in the chamber during the tunneling process, the earth pressures in different positions of the chamber are different and change with time constantly, which forms a 3D time-varying earth pressure field in the chamber. In addition, according to the classical earth pressure theory, the earth pressures in the different depths of the soil mass in front of the tunnel face are different and changing, as shown in Figure 3. This also forms a 3D time-varying earth pressure field in the soil mass in front of the tunnel face. Essentially, the interaction of the earth pressures on both sides of the tunnel face is caused by these two earth pressure fields, which determines the tunnel face stability. Therefore, to accurately reflect the influence of the earth pressures on the tunnel face, it is necessary to analyze the change situation of the earth pressures, model the earth pressure fields, and discover the new characteristics for tunnel face stability evaluation.

In order to evaluate the tunnel face stability reliably, this paper explores the description of the earth pressures in the chamber from a different point of view. Based on the earth pressures measured by the pressure sensors on the clapboard of the chamber, we construct a triangular mesh model for the earth pressure field by using optimization solution and projection Delaunay triangulation to fully reflect the change situation of the earth pressures in the chamber. Furthermore, the earth pressure field in the soil mass in front of the tunnel face is also analyzed and modeled in two limit equilibrium states (active equilibrium state and passive equilibrium state) by using the classical earth pressure theory. The normal vectors of the earth pressure field models can really reflect the change situations of the earth pressures both in the chamber and in the soil mass in front of the tunnel face. Therefore, it is a novel and effective way to use the normal vectors to describe the earth pressure

variation. The normal vector at each measuring point can concretely represent the variation degree of the local earth pressure field. Thus, we use the earth pressure field model and its normal vectors to design a new criterion for evaluating tunnel face stability in this paper.

The remainder of this paper is organized as follows: Section 2 describes the 2D projection Delaunay triangulation of the earth pressure field based on the measured earth pressures. Section 3 designs the evaluation criterion of tunnel face stability by using the triangular mesh model and the classical earth pressure theory. Section 4 presents method validation and analysis. Section 5 concludes our paper.

2. Earth pressure field modeling.

2.1. Earth pressure data processing. In order to accurately model the earth pressure field in the chamber, we should process the measured earth pressure data on the clapboard of the chamber at first. As we know, different types of EPB shield machines produced by different manufacturers have different number and arrangement of pressure sensors on the clapboard of the chamber. To present our modeling method more clearly, in this paper we choose a large-scale Herrenknecht EPB shield machine, which has been used for the Botlek Rail Tunnel in The Netherlands [7]. The diameter of this EPB shield machine is 9.75m, the length of its chamber is 1m, and 9 pressure sensors are installed on the clapboard of the chamber.

As shown in Figure 4, these 9 pressure sensors E1-E9 used to measure the earth pressures in the chamber are installed on the border area of the clapboard, since the rotation axis of the cutter head is installed on the center of the clapboard where the pressure sensors are impossible to be installed. In order to describe the earth pressure field integrally, we add several virtual earth pressure measuring points on the center area of the clapboard. The change mechanism of the earth pressure in the chamber is very important for estimating the earth pressures at the virtual points reliably. Through the real earth pressure data and their analysis by Bezuijen *et al.* [7], we know that the earth pressure increases linearly along the vertical direction (axis-y) from top to bottom in the rough. This is roughly in accord with the theory of the lithostatic pressure which states that the earth pressure increases linearly with the depth (as shown in Figure 3). As analyzed in the study [7], the major factor resulting in the earth pressure variation along the horizontal direction is the rotation of the cutter head. In general, the rotation of the cutter head will cause that there is more soil-water-foam mixture on one side than the other side of the chamber. This further causes that the earth pressure increases linearly along the horizontal direction from one side to the other side. This pressure variation along the horizontal direction is very small. Occasionally, the rotation of the cutter head may lead to the squeeze between the cutter head and the clapboard, which can cause that the earth pressure on one side of the chamber is a little higher than that on the other side of the chamber along the horizontal direction. Since the soil-water-foam mixture in the chamber is uniform and flowing, we can know that the earth pressure also changes gradually along the horizontal direction from one side to the other side in the situation. Therefore, considering the earth pressure variations along the vertical and horizontal directions synthetically, we know that the earth pressure field changes gradually and linearly in the chamber. As a result, in this paper, we will use the linear interpolation and linear fitting to estimate the earth pressures at the virtual pressure measuring points based on the real measured earth pressures.

Firstly, we add 5 virtual earth pressure measuring points A1, A2, A3, A4, and A5 along the tunnel axis, which are located on the lines E1E9, E2E8, E3E7, and E4E6 and on the horizontal position of E5 respectively, as shown in Figure 5. The earth pressures at A1, A2, A3, and A4 can be calculated by using the linear interpolations of the earth pressures at E1 and E9, E2 and E8, E3 and E7, and E4 and E6 respectively. And, the earth pressure at A5 is approximately equal to the earth pressure at E5, which makes a linear compensation for the influence of the screw conveyer. In addition, to describe the earth pressure field more integrally, we will add another 5 virtual earth pressure measuring points sequentially, that is, the origin D1 and the intersections D2, D3, D4, and D5 of the lines A3E2, A3E8, A3E6, and A3E4 with the inner circle, as shown in Figure 5. The earth pressure at D1 can be calculated by the linear fitting of the earth pressures at A1, A2, A3, A4, and A5. And, the earth pressures at D2, D3, D4, and D5 can be obtained by the linear interpolations of the earth pressures at A3 and E2, A3 and E8, A3 and E6, and A3 and E4. From the 9 real measuring points (E1-E9) and the 10 virtual measuring points (A1-A5 and D1-D5), we uniformly select 16 measuring points to construct the triangular model of the earth pressure field in the chamber, that is, E1-E9, A2, A4, and D1-D5, as shown in Figure 6.

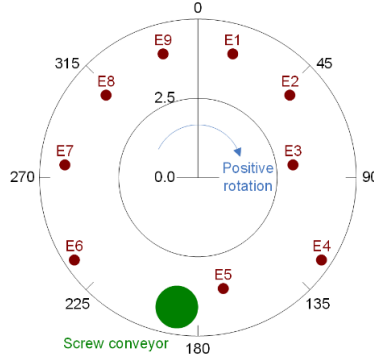


FIGURE 4. Pressure sensors on the clapboard.

In order to describe the earth pressure field, we establish a 3D Cartesian coordinate system $[O; x, y, z]$, where O is the center of the clapboard, x and y denote the position on the clapboard (unit: m), and z denotes the earth pressure (unit: bar), as shown in Figure 7. This coordinate system $[O; x, y, z]$ constructs a 3D earth pressure space. Therefore, if we have the earth pressures at the 16 measuring points, we can obtain 16 data points in the 3D earth pressure space. For example, the earth pressure at the measuring point $D1 = (x_{D1}, y_{D1})$ is $p_{e(D1)}$, and then we get the central point $(x_{D1}, y_{D1}, p_{e(D1)})$, which is also denoted by $\mathbf{p} = (x, y, z)$ for convenience. Similarly, we can get the other 15 points $(x_{E1}, y_{E1}, p_{e(E1)}) - (x_{E9}, y_{E9}, p_{e(E9)})$, $(x_{A2}, y_{A2}, p_{e(A2)})$, $(x_{A4}, y_{A4}, p_{e(A4)})$, and $(x_{D2}, y_{D2}, p_{e(D2)}) - (x_{D5}, y_{D5}, p_{e(D5)})$, which are regarded as the neighboring points of the central point \mathbf{p} and denoted by $\{\mathbf{p}_i = (x_i, y_i, z_i) | 1 \leq i \leq 15\}$. Finally, we obtain an original point set $P = \{\mathbf{p}, \mathbf{p}_i | 1 \leq i \leq 15\}$ of the earth pressures in 3D earth pressure space.

2.2. Optimization solution for the normal vector at the central point. In order to construct the triangular mesh model from the point set $P = \{\mathbf{p}, \mathbf{p}_i | 1 \leq$

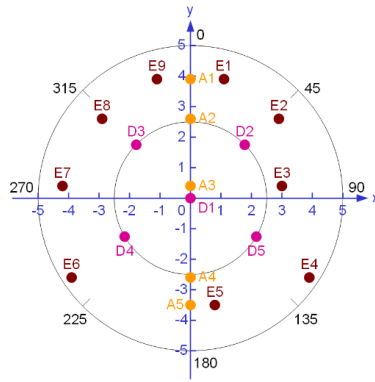


FIGURE 5. Virtual pressure measuring points.

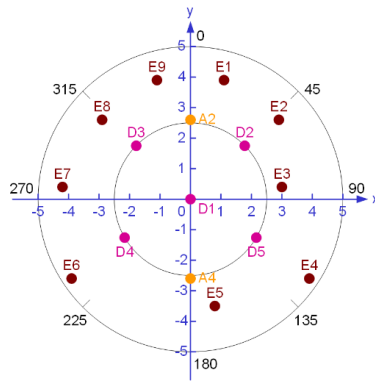


FIGURE 6. Measuring points used for modeling.

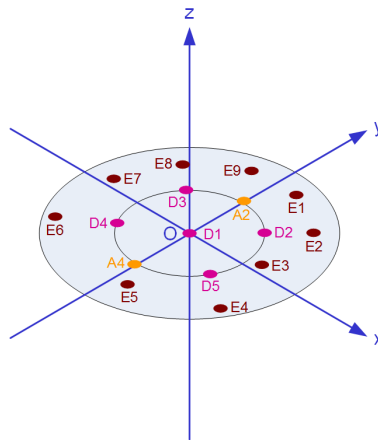


FIGURE 7. Coordinate system on the clapboard.

$i \leq 15\}$ of the earth pressures to describe the earth pressure field in the chamber, we estimate the normal vector to obtain the tangent plane at the central point \mathbf{p} . Let $\mathbf{p} = (x, y, z)$ denote the central point and $\{\mathbf{p}_i = (x_i, y_i, z_i) | 1 \leq i \leq 15\}$ denote the neighboring point of the central point $\mathbf{p} = (x, y, z)$, which are both on the earth pressure field surface S, as shown in Figure 8. Let $\mathbf{n} = (a, b, c)$ be the normal vector at the central point \mathbf{p} . Then, we would like to find the tangent plane $\mathbf{n} \cdot (\mathbf{p}_i - \mathbf{p}) = 0$ with $\mathbf{n} \cdot \mathbf{n} = 1$ at the central point \mathbf{p} such that the sum of square distances from the neighboring points \mathbf{p}_i to the tangent plane is minimized. This constrained optimization problem corresponding to the tangent plane at the central point \mathbf{p} can be described as follows

$$(P) \quad \min J(a, b, c) = \sum_{i=1}^{15} (a(x_i - x) + b(y_i - y) + c(z_i - z))^2, \quad (1)$$

$$s.t \quad a^2 + b^2 + c^2 = 1.$$

It can also be rewritten in the vector format

$$(P) \quad \min J(\mathbf{n}) = \sum_{i=1}^{15} (\mathbf{n} \cdot (\mathbf{p}_i - \mathbf{p}))^2, \quad (2)$$

$$s.t \quad \mathbf{n} \cdot \mathbf{n} = 1.$$

To solve this quadratic optimization problem, we need to construct the Lagrange function as follows

$$L(\mathbf{n}, \lambda) = \sum_{i=1}^{15} (\mathbf{n} \cdot (\mathbf{p}_i - \mathbf{p}))^2 + \lambda(\mathbf{n} \cdot \mathbf{n} - 1), \quad (3)$$

where λ is a Lagrange multiplier. The simultaneous equations for solving \mathbf{n} and λ are given by

$$\frac{\partial L}{\partial \mathbf{n}} = 0 \Rightarrow \left(\sum_{i=1}^{15} (\mathbf{p}_i - \mathbf{p})^T (\mathbf{p}_i - \mathbf{p}) \right) \mathbf{n}^T = \lambda \mathbf{n}^T, \quad (4)$$

$$\frac{\partial L}{\partial \lambda} = 0 \Rightarrow \mathbf{n} \mathbf{n}^T = 1.$$

Then, we have

$$J(\mathbf{n}) = \sum_{i=1}^{15} (\mathbf{n} \cdot (\mathbf{p}_i - \mathbf{p}))^2 = \mathbf{n} \left(\sum_{i=1}^{15} (\mathbf{p}_i - \mathbf{p})^T (\mathbf{p}_i - \mathbf{p}) \right) \mathbf{n}^T = \mathbf{n} \lambda \mathbf{n}^T = \lambda. \quad (5)$$

From (4), we know that the Lagrange multiplier λ is an eigenvalue of the 3×3 positive semi-definite matrix M

$$M = \sum_{i=1}^{15} (\mathbf{p}_i - \mathbf{p})^T (\mathbf{p}_i - \mathbf{p}) \quad (6)$$

with \mathbf{n}^T as the corresponding eigenvector. It is clear that to minimize $J(\mathbf{n})$, λ has to be the minimum eigenvalue of M. Therefore, the eigenvector corresponding to the minimum eigenvalue of M is the normal vector \mathbf{n} to the surface S at \mathbf{p} , as shown in Figure 9.

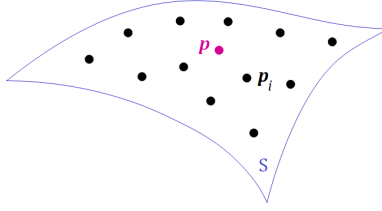


FIGURE 8. Discrete data points.

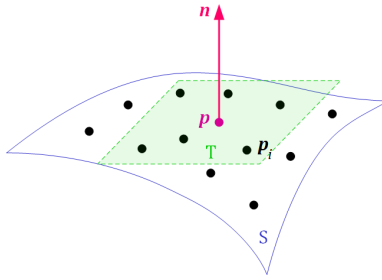


FIGURE 9. Normal vector and tangent plane at \mathbf{p} .

2.3. 2D projection of the data points. As we know, the neighboring point \mathbf{p}_i of the central point \mathbf{p} is on the surface S and out of the tangent plane T at \mathbf{p} . In order to achieve the 2D Delaunay triangulation locally, we project the neighboring point \mathbf{p}_i onto the tangent plane T perpendicularly along the normal vector \mathbf{n} . Thus, the projection $\bar{\mathbf{p}}_i$ of \mathbf{p}_i is given by

$$\bar{\mathbf{p}}_i = (\mathbf{p}_i - \mathbf{p}) - ((\mathbf{p}_i - \mathbf{p}) \cdot \mathbf{n}) \mathbf{n}, \quad (7)$$

as shown in Figure 10. Then, we can get the projection point set $\bar{P} = \{\bar{\mathbf{p}}, \bar{\mathbf{p}}_i | 1 \leq i \leq 15\}$ of the original point set $P = \{\mathbf{p}, \mathbf{p}_i | 1 \leq i \leq 15\}$, where $\bar{\mathbf{p}} = (0, 0, 0)$ is the projection of the central point \mathbf{p} onto the tangent plane T .

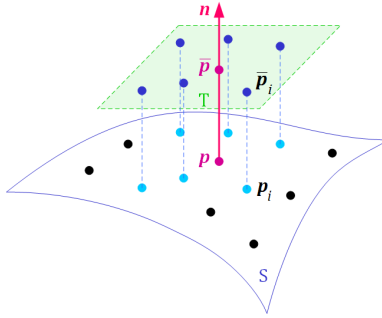


FIGURE 10. Projection of the data points onto the tangent plane.

2.4. 3D triangulation for the data points. In computational geometry, the 2D Delaunay triangulation for a set \bar{P} of discrete points in a plane is a triangulation $DT(\bar{P})$ such that no points in \bar{P} is inside the circumcircle of any triangle in $DT(\bar{P})$. Figure 11 shows the Delaunay triangulation (black triangular mesh) with all the circumcircles and their centers (red points). The Delaunay triangulation maximizes the minimum angle of all the angles of the triangles, and it tends to avoid thin triangles. The Delaunay triangulation has the following advantages: 1) the union of all simplices in the Delaunay triangulation is the convex hull of the points; 2) the closest three points form a triangle in the Delaunay triangulation and the sides of the triangles do not intersect; 3) wherever the Delaunay triangulation begins, a same result is obtained; 4) the addition, deletion, or movement of a vertex in the Delaunay triangulation only affects its neighboring triangles. Therefore, it can describe the geometric model of discrete points accurately, uniquely, and optimally. The Delaunay triangulation $DT(\bar{P})$ for a set \bar{P} of discrete points corresponds to the dual graph of the Voronoi diagram $VD(\bar{P})$ for \bar{P} , as shown in Figure 12.

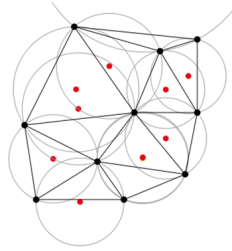


FIGURE 11. Delaunay triangulation.

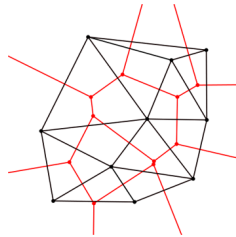


FIGURE 12. Voronoi diagram.

Many algorithms are proposed for computing the Delaunay triangulation, such as the flip method, incremental algorithm, divide and conquer algorithm, sweepline method, and sweep hull method. Different methods have different time complexities. In this paper, we use a randomized incremental algorithm to compute the Delaunay triangulation directly from the discrete points. For details, see the book [6]. By using this method, we obtain the 2D Delaunay triangular mesh $DT(\bar{P})$ for the projection point set $\bar{P} = \{\bar{p}, \bar{p}_i | 1 \leq i \leq 15\}$ on the tangent plane T , and then we project this 2D triangular relationship to the 3D surface S reversely. As a result, we get the 3D triangular mesh $TM(P)$ constructed by the original point set $P = \{p, p_i | 1 \leq i \leq 15\}$, as shown in Figure 13. Therefore, for the earth pressures in

the chamber, we can construct their 3D triangular mesh model $TM(P)$ to describe the earth pressure field in the chamber.

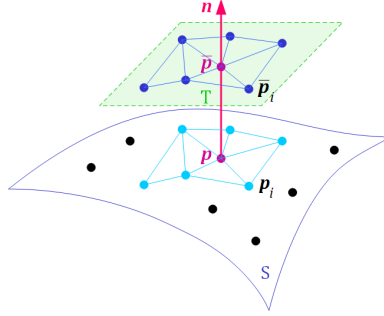


FIGURE 13. 3D triangulation for the data points.

2.5. Estimation of the normal vectors at the data points. When we get the 3D triangular mesh of the data points, we will recalculate the normal vector \mathbf{n} at the central point \mathbf{p} by using the normal vectors $\{\mathbf{t}_m | 1 \leq m \leq \bar{n}\}$ of its adjacent triangles as follows

$$\mathbf{n} = \sum_{m=1}^{\bar{n}} \mathbf{t}_m / \left| \sum_{m=1}^{\bar{n}} \mathbf{t}_m \right|. \quad (8)$$

where \bar{n} is the number of the adjacent triangles and \mathbf{t}_m is the normal vector of each adjacent triangle. In the same way, we can also compute the normal vector \mathbf{n}_i at the neighboring point \mathbf{p}_i , as shown in Figure 14. The normal vectors \mathbf{n} and \mathbf{n}_i will be used to establish the evaluation criterion and evaluate the tunnel face stability.

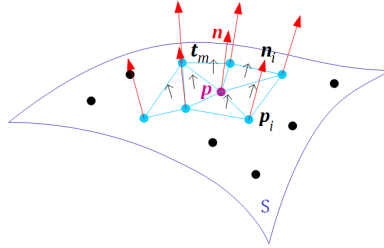


FIGURE 14. Normal vectors at the data points.

3. Tunnel face stability evaluation.

3.1. Active and passive earth pressures. During the tunneling process, the earth pressure in the chamber must balance the external earth and hydrostatic pressures in order to maintain tunnel face stability. If the earth pressure in the chamber decreases gradually, the tunnel face will produce a movement tendency towards the chamber and away from the soil mass. Then, the horizontal stress of the soil mass in front of the tunnel face also decreases accordingly. If the horizontal stress of the soil mass decreases to the minimum value, a state of plastic limit

equilibrium is reached, and the soil mass in front of the tunnel face will undergo an active failure (collapse). The horizontal stress at this situation is defined as the active earth pressure p_a (kPa). According to Rankine's theory of earth pressure [24, 26], the active earth pressure can be obtained by

$$p_a = K_a \gamma h - 2c\sqrt{K_a}, \quad (9)$$

where K_a is the active earth pressure coefficient, γ is the volume-weight of the soil (kN/m^3), h is the depth from the calculation point to the earth surface (m), and c is the cohesion force of the soil (kN/m^2). The active earth pressure coefficient K_a is given by

$$K_a = \frac{1 - \sin \varphi}{1 + \sin \varphi} = \tan^2 (45^\circ - \varphi/2), \quad (10)$$

where φ is the internal friction angle of the soil. Therefore, the active earth pressure can be rewritten as

$$p_a = \gamma h \tan^2 (45^\circ - \varphi/2) - 2c \tan (45^\circ - \varphi/2). \quad (11)$$

Conversely, if the earth pressure in the chamber increases gradually, the tunnel face will produce a movement tendency towards the soil mass and away from the chamber. Then, the horizontal stress of the soil mass in front of the tunnel face also increases accordingly. If the horizontal stress of the soil mass increases to the maximum value, another state of plastic limit equilibrium is reached, and the soil mass in front of the tunnel face will undergo a passive failure (blow-out). The horizontal stress at this situation is defined as the passive earth pressure p_p (kPa) given by

$$p_p = K_p \gamma h + 2c\sqrt{K_p}, \quad (12)$$

where K_p is the passive earth pressure coefficient and is calculated by

$$K_p = \frac{1 + \sin \varphi}{1 - \sin \varphi} = \tan^2 (45^\circ + \varphi/2). \quad (13)$$

Therefore, the passive earth pressure can be rewritten as

$$p_p = \gamma h \tan^2 (45^\circ + \varphi/2) + 2c \tan (45^\circ + \varphi/2). \quad (14)$$

3.2. Earth pressure fields. The equations above show that both the active and passive earth pressures change with the depth, which will form an active earth pressure field and a passive earth pressure field in the soil mass in front of the tunnel face respectively. In order to describe the active and passive earth pressure fields more clearly, we establish a 3D Cartesian coordinate system $[O; x, y, z]$ in the soil mass in front of the tunnel face, where O is the center of the cutter head, x denotes the horizontal position of the cutter head, y denotes the vertical position of the cutter head, and z denotes the earth pressure whose unit is set to bar according to the pressure sensors on the clapboard of the chamber. According to Rankine's theory, the units of the active earth pressure p_a and the passive earth pressure p_p are kPa. Therefore, in order to analysis the active and passive earth pressures in the coordinate system $[O; x, y, z]$, we must transform kPa to bar. As we know, 1bar=100kPa. Then, we have $z_{\text{bar}}=100z_{\text{kPa}}$. Thus, $p_a = 100z$ and $p_p = 100z$. Let $h = H - y$, where H is the distance from the center of the cutter head to the earth surface. Therefore, according to (11), the active earth pressure can be described as

$$100z = \gamma H \tan^2 (45^\circ - \varphi/2) - \gamma y \tan^2 (45^\circ - \varphi/2) - 2c \tan (45^\circ - \varphi/2). \quad (15)$$

Then, we have

$$100z + \gamma \tan^2(45^\circ - \varphi/2)y - \gamma H \tan^2(45^\circ - \varphi/2) + 2c \tan(45^\circ - \varphi/2) = 0. \quad (16)$$

This equation indicates that the active earth pressure field is an inclined plane. And, we can get its normal vector by

$$\mathbf{n}_a = \frac{(0, \gamma \tan^2(45^\circ - \varphi/2), 100)}{|(0, \gamma \tan^2(45^\circ - \varphi/2), 100)|}. \quad (17)$$

Then, we calculate the angle θ_a between the normal vector \mathbf{n}_a and the coordinate plane- xy , also called the *active earth pressure angle*, as follows

$$\theta_a = \tan^{-1} \frac{100}{\gamma \tan^2(45^\circ - \varphi/2)}, \quad (18)$$

which represents the variation degree of the active earth pressure field relative to the coordinate plane- xy . Similarly, according to (14), the passive earth pressure can be described as

$$100z = \gamma H \tan^2(45^\circ + \varphi/2) - \gamma y \tan^2(45^\circ + \varphi/2) + 2c \tan(45^\circ + \varphi/2). \quad (19)$$

Then, we have

$$100z + \gamma \tan^2(45^\circ + \varphi/2)y - \gamma H \tan^2(45^\circ + \varphi/2) - 2c \tan(45^\circ + \varphi/2) = 0. \quad (20)$$

This equation indicates that the passive earth pressure field is also an inclined plane. And, we can get its normal vector by

$$\mathbf{n}_p = \frac{(0, \gamma \tan^2(45^\circ + \varphi/2), 100)}{|(0, \gamma \tan^2(45^\circ + \varphi/2), 100)|}. \quad (21)$$

Then, we calculate the angle θ_p between the normal vector \mathbf{n}_p and the coordinate plane- xy , also called the *passive earth pressure angle*, as follows

$$\theta_p = \tan^{-1} \frac{100}{\gamma \tan^2(45^\circ + \varphi/2)}, \quad (22)$$

which represents the variation degree of the passive earth pressure field relative to the coordinate plane- xy .

Figure 15 shows the active and passive earth pressure fields, their normal vectors, and the active and passive earth pressure angles. The area EA between the active earth pressure field and the passive earth pressure field is defined as the *effective pressure area* (the green area in Figure 15).

3.3. Stability evaluation. During the tunneling process, the earth pressures in the chamber are measured in real time by the pressure sensors installed on the clapboard. By using the measured earth pressures, we can obtain the original point set $P = \{\mathbf{p}, \mathbf{p}_i | 1 \leq i \leq 15\}$ and construct the triangular mesh model of the earth pressure field in the chamber based on our 2D projection Delaunay triangulation method. We can also estimate the normal vector \mathbf{n} at \mathbf{p} and the normal vector \mathbf{n}_i at \mathbf{p}_i , and calculate the angle θ between \mathbf{n} and plane- xy and the angle θ_i between \mathbf{n}_i and plane- xy . The angles θ and θ_i are called the *earth pressure angles* at \mathbf{p} and \mathbf{p}_i , which represent the variation degrees of the local earth pressure fields relative to the coordinate plane- xy . At any given moment of the tunneling process, only if the earth pressure is between the active earth pressure and the passive earth pressure and the earth pressure field changes gradually in any position of the chamber, will

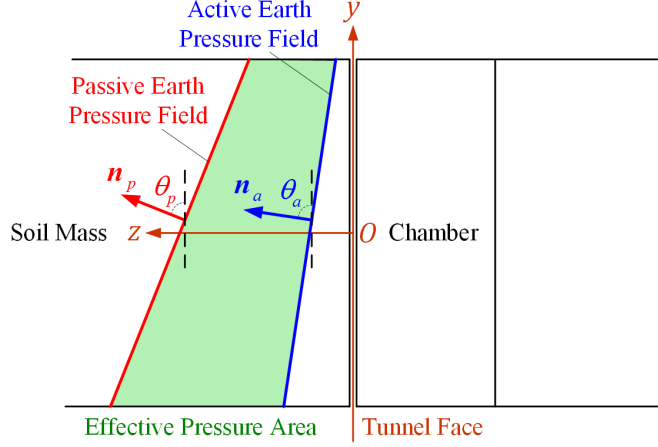


FIGURE 15. Active and passive earth pressure fields.

the tunnel face be stable. Now, we give the evaluation criterion of tunnel face stability for the EPB shield machine.

Evaluation criterion. Let $TM(P)$ be the triangular mesh model of the earth pressure field in the chamber, which is constructed by using the original point set $P = \{\mathbf{p}, \mathbf{p}_i | 1 \leq i \leq 15\}$ of the earth pressures. The angles θ and θ_i are the earth pressure angles at \mathbf{p} and \mathbf{p}_i . If and only if the two following conditions are met simultaneously, the tunnel face is stable.

- (1) All data points are in the effective pressure area, that is, $\mathbf{p} \in EA$ and $\mathbf{p}_i \in EA$.
- (2) All earth pressure angles are between the passive earth pressure angle and the active earth pressure angle, that is, $\theta_p < \theta < \theta_a$ and $\theta_p < \theta_i < \theta_a$.

When we evaluate tunnel face stability, we consider not only the value of the earth pressure but also the variation degree of the earth pressure in any position of the chamber. Only when both of them meet the conditions can the tunnel face be stable.

4. Method validation and analysis. In order to show the performance of our method, we experiment with the real earth pressure data measured by the Herrenknecht EPB shield machine, which was used for the Botlek Rail Tunnel in The Netherlands [7]. The diameter of this EPB shield machine is 9.75m, the length of its chamber is 1m, and the distance H from the center of the cutter head to the earth surface is 30m. 9 pressure sensors are installed on the clapboard of the chamber for measuring the earth pressures, as shown in Figure 4. The span of the pressure sensors is 0~6 bar, and the accuracy of the pressure sensors is 0.25% of span. The geology of the bored tunnel is Pleistocene sand, the volume-weight γ of the soil is about 18.62 kN/m³, the cohesion force c of the soil is 5.1 kN/m², and the internal friction angle φ of the soil is 36°. Therefore, the active earth pressure field is $100z + 4.83y - 139.82 = 0$ and the passive earth pressure field is $100z + 71.72y - 2171.66 = 0$. The unit normal vectors of the active and passive earth pressure fields are computed as $\mathbf{n}_a = (0, 0.0483, 0.9988)$ and $\mathbf{n}_p = (0, 0.5828, 0.8126)$. And, the active and passive earth pressure angles are $\theta_a = 87.2^\circ$ and $\theta_p = 54.3^\circ$.

Figure 16 presents the constructed triangular mesh models and the estimated normal vectors by using six groups of earth pressures measured at six different times during the normal tunneling process. As can be observed, all data points are in the effective pressure area at each moment, which indicates the earth pressures are between the active earth pressure and the passive earth pressure in all positions of the chamber at each moment. Table 1 shows the earth pressure angles at the measuring points for the six groups of earth pressures measured at six different times. From Figure 16 and Table 1, We can find that all earth pressure angles are between the passive earth pressure angle and the active earth pressure angle at each moment, which indicates the local earth pressure fields change gradually in all positions of the chamber at each moment. According to the evaluation criterion of tunnel face stability, the earth pressure field in the chamber meets the two conditions simultaneously, and therefore the tunnel face is stable at each moment during the normal tunneling process, which is in accord with the actual tunneling situation.

TABLE 1. Earth pressure angles at the measuring points (unit: $^{\circ}$)

Time No.	E1	E2	E3	E4	E5	E6	E7	E8
1	82.1263	79.4182	80.7525	81.1181	79.9521	82.2279	81.4088	79.1411
2	80.8168	79.9801	79.9147	80.0957	79.1641	80.9488	80.3536	78.8670
3	82.6131	81.7718	80.6488	79.9071	79.0446	80.1266	80.7302	81.9452
4	78.8249	77.6968	77.2621	78.0584	79.1200	79.5718	77.7454	76.5422
5	78.5580	79.0929	78.1572	78.2970	79.4725	79.8513	78.4722	77.3459
6	79.7876	79.6536	78.4048	77.4864	78.4145	78.0623	78.3591	79.8496
Time No.	E9	A2	A4	D1	D2	D3	D4	D5
1	82.3057	80.8872	81.9276	81.2639	80.2467	80.4916	82.5693	81.9542
2	81.7089	80.2221	80.5088	80.1633	79.8461	79.8634	81.1366	80.1815
3	84.9260	82.4601	79.8087	80.5708	81.6030	81.6349	80.6627	79.5281
4	80.5892	78.1447	78.9757	77.5015	77.4125	77.5080	78.5850	78.0865
5	79.9673	78.5516	79.1212	78.2072	78.6575	78.2354	78.9935	77.9871
6	81.2070	79.9441	77.7178	78.2115	79.841	79.2915	77.8964	77.0773

In the normal working condition, the earth pressures in the chamber change very little when the tunnel face is stable. There are several critical factors which will influence the earth pressures in the chamber, such as the screw conveyer speed, advance speed, and cutter head speed. In these operating parameters, the screw conveyer speed has a significant influence on the earth pressures in the chamber. If the screw conveyer speed is higher, the soil mass discharged out of the chamber is larger than that cut into the chamber, and the earth pressures in the chamber will decrease. If the screw conveyer speed is lower, the soil mass discharged out of the chamber is smaller than that cut into the chamber, and the earth pressures in the chamber will increase. Therefore, we can simulate the earth pressure variation in the chamber through controlling the screw conveyer speed to adjust the discharged soil mass. Since the pressure sensor E5 is closest to the screw conveyer, the earth pressure measured by the pressure sensor E5 can directly reflect the earth pressure variation caused by the screw conveyer speed, as shown in Figure 4. Therefore, we assume that the earth pressure measured by the pressure sensor E5 changes with the screw conveyer speed and the other measured earth pressures remain unchanged, and then we analyze the tunnel face stability in this situation.

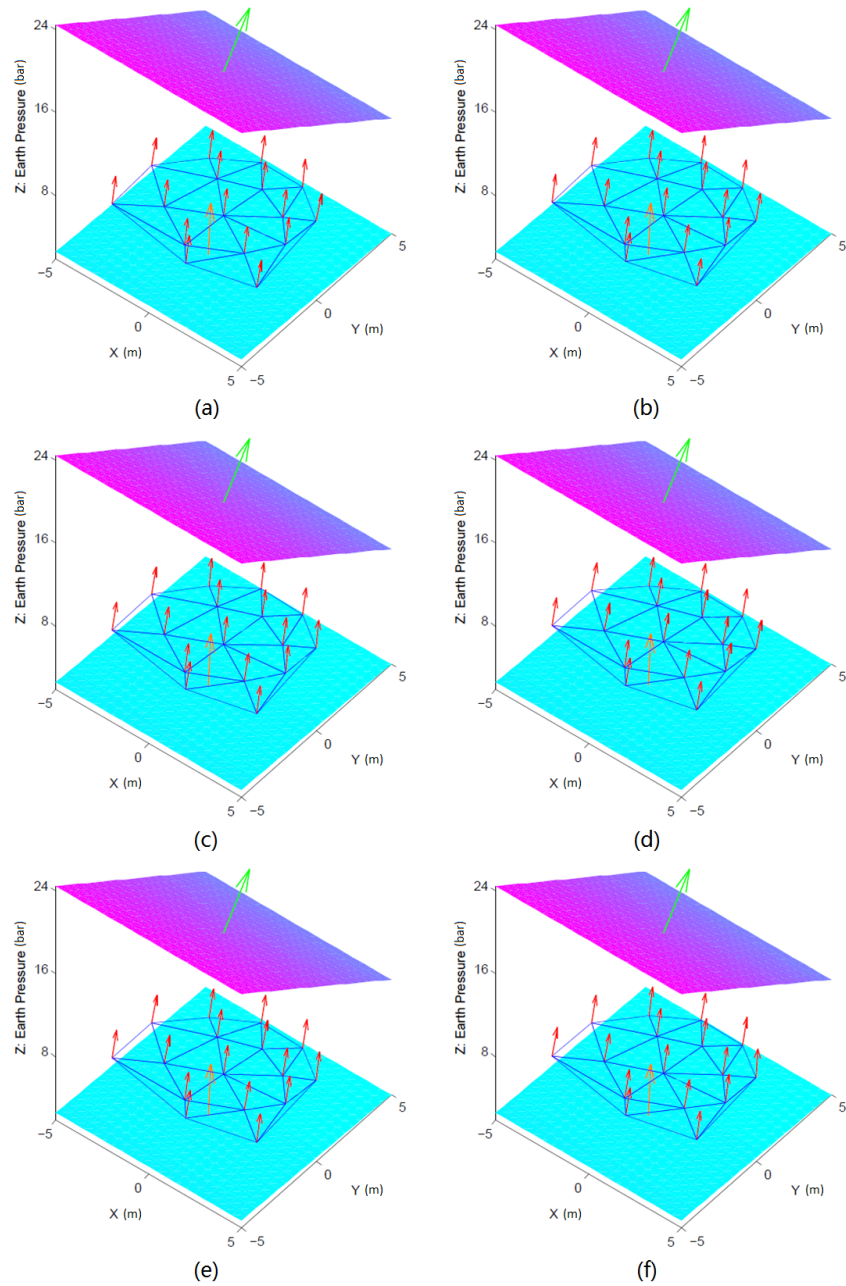


FIGURE 16. Earth pressure fields at six different times (a)-(f). The cyan and blue violet planes denote the active and passive earth pressure fields, the orange and green arrows denote the normal vectors of the active and passive earth pressure fields, the blue triangular meshes denote the earth pressure fields, and the red arrows denote the normal vectors at the measuring points. The units of the axes x and y are meter and the unit of the axis z is bar.

Figure 17 presents the simulation result and shows the earth pressure angle with the earth pressure changing from 80% to 140% of the normal earth pressure p_{ne} at the measuring point E5. In this situation, all the earth pressures in the chamber are between the active earth pressure and the passive earth pressure, which meets the first condition of the evaluation criterion. In the following, we mainly analyze the influence of the earth pressure angle at E5 on the tunnel face stability.

(1) The earth pressure at E5 increases 4%, which simulates the screw conveyer speed and the soil mass discharged out of the chamber decrease small. In this situation, the earth pressure angle at E5 is 69.8° and is between the active earth pressure angle and the passive earth pressure angle. This means that the local variation degree of the earth pressure near E5 is small. Therefore, the tunnel face is stable and the blow-out would not happen.

(2) The earth pressure at E5 increases 16%, which simulates the screw conveyer speed and the soil mass discharged out of the chamber decrease large. In this situation, the earth pressure angle at E5 is 56.4° and is very close to the passive earth pressure angle. This means that the local variation degree of the earth pressure near E5 is large. Therefore, the tunnel face is under a limit equilibrium state and the blow-out would happen soon.

(3) The earth pressure at E5 increases 30%, which simulates the screw conveyer speed and the soil mass discharged out of the chamber decrease very large. In this situation, the earth pressure angle at E5 is 44.1° and is lower than the passive earth pressure angle. This means that the local variation degree of the earth pressure near E5 is very large. Therefore, the tunnel face is locally unstable and the blow-out has already happened.

(4) The earth pressure at E5 decreases 4%, which simulates the screw conveyer speed and the soil mass discharged out of the chamber increase small. In this situation, the earth pressure angle at E5 is 80.1° and is between the active earth pressure angle and the passive earth pressure angle. This means that the local variation degree of the earth pressure near E5 is small. Therefore, the tunnel face is stable and the collapse would not happen.

(5) The earth pressure at E5 decreases 8%, which simulates the screw conveyer speed and the soil mass discharged out of the chamber increase large. In this situation, the earth pressure angle at E5 is 85.1° and is very close to the active earth pressure angle. This means that the local variation degree of the earth pressure near E5 is large. Therefore, the tunnel face is under a limit equilibrium state and the collapse would happen soon.

(6) The earth pressure at E5 decreases 20%, which simulates the screw conveyer speed and the soil mass discharged out of the chamber increase very large. In this situation, the earth pressure angle at E5 is 99.9° and is higher than the active earth pressure angle. This means that the local variation degree of the earth pressure near E5 is very large. Therefore, the tunnel face is locally unstable and the collapse has already happened.

Figure 18 shows the constructed triangular mesh models and the estimated normal vectors when the earth pressure at E5 decreases to $50\%p_{ne}$ and increases to $150\%p_{ne}$ respectively. In these two cases, the earth pressure angles are above the active earth pressure angle and below the passive earth pressure angle respectively, which indicates the local earth pressure field at E5 changes suddenly. Therefore, the tunnel face is locally unstable.

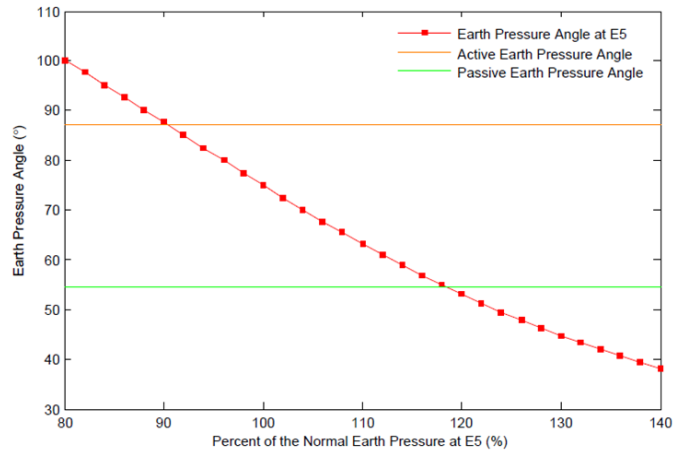


FIGURE 17. Earth pressure angle with the varying earth pressure at E5.

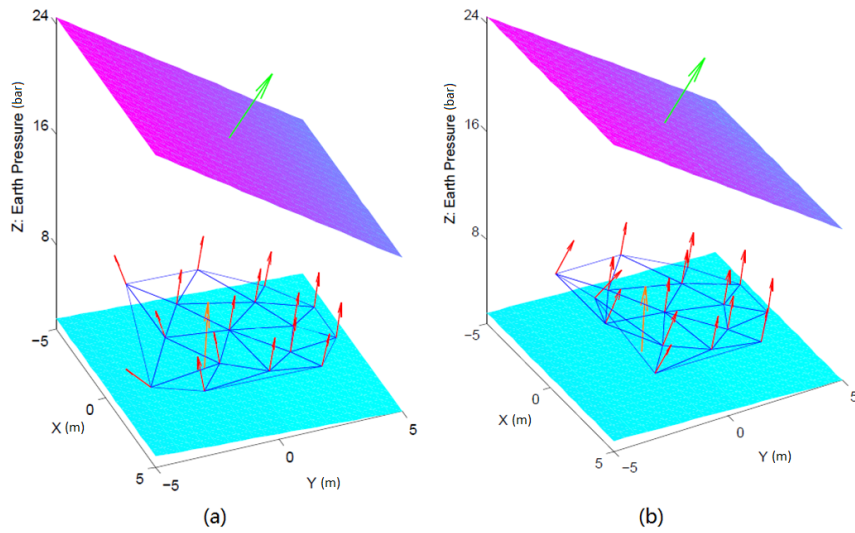


FIGURE 18. Earth pressure fields in two cases. (a) The earth pressure at E5 decreases to $50\%p_{ne}$. (b) The earth pressure at E5 increases to $150\%p_{ne}$. The units of the axes x and y are meter and the unit of the axis z is bar.

5. **Conclusion.** This paper presents a novel earth pressure field modeling approach to evaluate the tunnel face stability of large and complex EPB shield machines. Based on the earth pressures measured by the pressure sensors on the clapboard of the chamber, a triangular mesh model of the earth pressure field is constructed by using optimization solution and projection Delaunay triangulation to fully reflect the change situation of the earth pressures in the chamber. By using the triangular mesh model of the earth pressure field, the normal vector at each measuring point

is estimated, which can accurately reflect the variation degree of the local earth pressure field. Furthermore, Rankine's theory is used to determine the active and passive earth pressure fields and compute their normal vectors in the limit equilibrium states respectively. Combining the active and passive Rankine states, the triangular mesh model of the earth pressure field and its normal vectors are deployed to design a new criterion for evaluating tunnel face stability. The method validation and analysis demonstrate that the proposed method is effective for modeling the earth pressure field in the chamber and evaluating the tunnel face stability for EPB shield machines.

Since the EPB shield machine is a very complex system, the earth pressure in the chamber may be influenced by different kinds of factors, such as the cutter head rotation, the screw conveyer rotation, and the geological condition. In the future, more real field data from the tunnel excavation projects will be used to analyze the variation characteristics of the earth pressure field in the chamber and validate the proposed method further.

Acknowledgments. This work is supported by the National Natural Science Foundation of China under Grant 61673083, by the Fundamental Research Funds for the Central Universities under Grant DUT17LAB01, and by Natural Science Foundation of Liaoning Province under Grant 20170540167.

REFERENCES

- [1] M. Ahmed and M. Iskander, [Evaluation of tunnel face stability by transparent soil models](#), *Tunnelling and Underground Space Technology*, **27** (2012), 101–110.
- [2] G. Anagnostou and K. Kovári, [The face stability of slurry-shield-driven tunnels](#), *Tunnelling and Underground Space Technology*, **9** (1994), 165–174.
- [3] G. Anagnostou and K. Kovári, [Face stability conditions with earth-pressure-balanced shields](#), *Tunnelling and Underground Space Technology*, **11** (1996), 165–173.
- [4] J. H. Atkinson and D. M. Potts, [Stability of a shallow circular tunnel in cohesionless soil](#), *Géotechnique*, **27** (1977), 203–215.
- [5] C. E. Augarde, A. V. Lyamin and S. W. Sloan, [Stability of an undrained plane strain heading revisited](#), *Computers and Geotechnics*, **30** (2003), 419–430.
- [6] M. D. Berg, O. Cheong, M. V. Kreveld and M. Overmars, *Computational Geometry: Algorithms and Applications*, Berlin and Heidelberg: Springer, 2008.
- [7] A. Bezuijen, A. M. Talmon, J. F. W. Joustra and B. Grote, [Pressure gradients at the EPBM face](#), *Tunnels and Tunnelling International*, **37** (2005), 14–17.
- [8] R. I. Borja, [A finite element model for strain localization analysis of strongly discontinuous fields based on standard Galerkin approximation](#), *Computer Methods in Applied Mechanics and Engineering*, **190** (2000), 1529–1549.
- [9] W. Broere, *Tunnel Face Stability and New CPT Applications*, Ph.D thesis, Delft University of Technology in Delft, 2001.
- [10] P. Chambon and J.-F. Corté, [Shallow tunnels in cohesionless soil: Stability of tunnel face](#), *Journal of Geotechnical Engineering*, **120** (1994), 1148–1165.
- [11] R. P. Chen, L. J. Tang, D. S. Ling and Y. M. Chen, [Face stability analysis of shallow shield tunnels in dry sandy ground using the discrete element method](#), *Computers and Geotechnics*, **38** (2011), 187–195.
- [12] E. H. Davis, M. J. Gunn, R. J. Mair and H. N. Seneviratne, [The stability of shallow tunnels and underground openings in cohesive material](#), *Géotechnique*, **30** (1980), 397–416.
- [13] M. Huang, S. Li, J. Yu and J. Q. W. Tan, [Continuous field based upper bound analysis for three-dimensional tunnel face stability in undrained clay](#), *Computers and Geotechnics*, **94** (2018), 207–213.
- [14] E. Ibrahim, A.-H. Soubra, G. Mollon, W. Raphael, D. Dias and A. Reda, [Three-dimensional face stability analysis of pressurized tunnels driven in a multilayered purely frictional medium](#), *Tunnelling and Underground Space Technology*, **49** (2015), 18–34.

- [15] S. Jancsecz and W. Steiner, [Face support for a large Mix-Shield in heterogeneous ground conditions](#), *Tunnelling'94*, (1994), 531–550.
- [16] A. M. Karim, *Three-dimensional Discrete Element Modeling of Tunneling in Sand*, Ph.D thesis, University of Alberta in Edmonton, 2007.
- [17] S. H. Kim and F. Tonon, [Face stability and required support pressure for TBM driven tunnels with ideal face membrane-Drained case](#), *Tunnelling and Underground Space Technology*, **25** (2010), 526–542.
- [18] A. Kirsch, [Experimental investigation of the face stability of shallow tunnels in sand](#), *Acta Geotechnica*, **5** (2010), 43–62.
- [19] E. Leca and L. Dormieux, [Upper and lower bound solutions for the face stability of shallow circular tunnels in frictional material](#), *Géotechnique*, **40** (1990), 581–606.
- [20] Y. Li, F. Emeriault, R. Kastner and Z. X. Zhang, [Stability analysis of large slurry shield-driven tunnel in soft clay](#), *Tunnelling and Underground Space Technology*, **24** (2009), 472–481.
- [21] X. Lü, Y. Zhou, M. Huang and S. Zeng, [Experimental study of the face stability of shield tunnel in sands under seepage condition](#), *Tunnelling and Underground Space Technology*, **74** (2018), 195–205.
- [22] K. Michael, L. Dimitris, V. Ioannis and F. Petros, [Development of a 3D finite element model for shield EPB tunnelling](#), *Tunnelling and Underground Space Technology*, **65** (2017), 22–34.
- [23] Q. Pan and D. Dias, [Three dimensional face stability of a tunnel in weak rock masses subjected to seepage forces](#), *Tunnelling and Underground Space Technology*, **71** (2018), 555–566.
- [24] W. J. M. Rankine, [On the Stability of Loose Earth](#), *Philosophical Transactions of The Royal Society of London*, **147** (1857), 9–27.
- [25] H. Schuller and H. F. Schweiger, [Application of a Multilaminat Model to simulation of shear band formation in NATM-tunnelling](#), *Computers and Geotechnics*, **29** (2002), 501–524.
- [26] C. Shao and D. S. Lan, [Tunnel face stability analysis based on pressure field surface's normal vector for earth pressure balanced shield](#), *International Journal of Modelling Identification and Control*, **17** (2012), 143–150.
- [27] C. Shao and D. S. Lan, [Optimal control of an earth pressure balance shield with tunnel face stability](#), *Automation in Construction*, **46** (2014), 22–29.

Received June 2018; revised September 2018.

E-mail address: anyi@dlut.edu.cn

E-mail address: ladaola@dlut.edu.cn

E-mail address: changzhiwu@gzhu.edu.cn

E-mail address: hhu@essex.ac.uk

E-mail address: cshao@dlut.edu.cn

E-mail address: libo19951218@mail.dlut.edu.cn